PHYSICAL REVIEW D **91,** 035015 (2015)

Exploring resonant di-Higgs boson production in the Higgs singlet model

Chien-Yi Chen,[1] S. Dawson,[1] and I. M. Lewis[1,2]

[1]*Department of Physics, Brookhaven National Laboratory, Upton, New York 11973, USA*

[2]*SLAC National Accelerator Laboratory, 2575 Sand Hill Rd, Menlo Park, California 94025, USA*

(Received 28 October 2014; published 13 February 2015)

We study the enhancement of the di-Higgs production cross section resulting from the resonant decay of a heavy Higgs boson at hadron colliders in a model with a Higgs singlet. This enhancement of the double Higgs production rate is crucial in understanding the structure of the scalar potential and we determine the maximum allowed enhancement such that the electroweak minimum is a global minimum. The di-Higgs production enhancement can be as large as a factor of $\sim 18(13)$ for the mass of the heavy Higgs around 270(420) GeV relative to the Standard Model rate at 14 TeV for parameters corresponding to a global electroweak minimum.

DOI: 10.1103/PhysRevD.91.035015 PACS numbers: 12.60.Fr, 12.60.-i, 14.80.Ec

I. INTRODUCTION

After the discovery of the Higgs boson, the next task is to determine its couplings to as many Standard Model (SM) particles as possible. Only by doing so can the true nature of electroweak symmetry breaking be determined. It is particularly important to measure the parameters of the scalar potential, which entails measuring double Higgs production [1–3]. In the SM, this rate is small at the LHC [4–9], but may be significantly enhanced in models with new physics. One simple extension of the SM is to add a scalar, S, which is a singlet under all the gauge symmetries [10–13]. After electroweak symmetry breaking, S can mix with the SM Higgs boson, leading to a modification of Higgs couplings to SM particles and to the parameters of the scalar potential. In such models, there can be an enhancement of the di-Higgs rate due to the resonant production of the new scalar [14–16].

Models with a Higgs singlet are highly motivated by Higgs portal models [17–19]. In such models, S is the only particle which couples to a dark matter sector. Couplings of the dark matter to the known particles occur only through the mixing of S with the SM Higgs boson. If the Higgs singlet model possesses a Z_2 symmetry, the scalar singlet itself could be a dark matter candidate. Without a Z_2 symmetry, cubic and linear self-coupling terms are allowed in the scalar potential and a strong first order electroweak phase transition is allowed. Motivated by the possibility of explaining electroweak baryogenesis [20–22], we examine enhanced double Higgs production in a model with a scalar singlet and no Z_2 symmetry. The requirement that the electroweak minimum be a global minimum provides stringent restrictions on the allowed parameter space.

Attempts to increase the di-Higgs production rate by adding new particles which contribute to double Higgs production from gluon fusion have generally not found increases of more than a factor of 2–3 over the SM rate [23–25]. More successful has been the study of resonant enhancements, where increases up to a factor of ~ 50 relative to the SM prediction for double Higgs production have been found in 2 Higgs doublet models and the MSSM [26–30]. We determine the maximum allowed enhancement from resonant di-Higgs production in the singlet model without a Z_2 symmetry [31], such that the parameters correspond to a global electroweak minimum [21]. This case has a number of novel features in comparison with the well studied Z_2 symmetric singlet model [10].

In Sec. II, we review the Higgs singlet model and the minimization of the potential. Our results for the maximum allowed enhancement of the di-Higgs cross section, subject to the restriction that the electroweak minimum be a global minimum, are in Sec. III. Experimental constraints and theoretical restrictions on the parameters are given in Sec. IV. We include 2 appendices: Appendix A has the complete set of cubic and quartic Higgs self-couplings and Appendix B includes a description of the vacuum with $v = 0$.

II. MODEL

We consider a model containing the SM Higgs doublet, H, and an additional Higgs singlet, S. The most general scalar potential is

$$V(H,S) = V_H(H) + V_{HS}(H,S) + V_S(S), \tag{1}$$

with

$$V_H(H) = -\mu^2 H^\dagger H + \lambda (H^\dagger H)^2 \tag{2}$$

$$V_{HS}(H,S) = \frac{a_1}{2} H^\dagger H S + \frac{a_2}{2} H^\dagger H S^2 \tag{3}$$

$$V_S(S) = b_1 S + \frac{b_2}{2} S^2 + \frac{b_3}{3} S^3 + \frac{b_4}{4} S^4. \tag{4}$$

We do not assume a Z_2 symmetry which would prohibit a_1, b_1 and b_3. The neutral component of the doublet H is denoted by $\phi_0 = (h+v)/\sqrt{2}$, where the vacuum expectation value (vev) is $\langle\phi_0\rangle = \frac{v}{\sqrt{2}}$. Similarly, the vev of S is defined as x.

The extrema of the potential are obtained by requiring $\partial V(v,x)/\partial v = 0$ and $\partial V(v,x)/\partial x = 0$,[1]

$$\frac{v}{2}(-2\mu^2 + 2\lambda v^2 + a_1 x + a_2 x^2) = 0, \tag{5}$$

$$x\left(b_2 + b_3 x + b_4 x^2 + \frac{v^2}{2}a_2\right) + b_1 + \frac{v^2}{4}a_1 = 0. \tag{6}$$

Solving Eqs. (5) and (6) produce many possible extrema of the potential. We require that one of these extrema correspond to the electroweak symmetry breaking (EWSB) minimum, $v = v_{\rm EW} = 246$ GeV. It is important to note that a shift of the singlet field by $S \to S + \Delta_S$ is just a redefinition of the parameters of Eq. (4) and does not change the physics. Hence, we are free to choose our EWSB minimum as $(v,x) \equiv (v_{\rm EW}, 0)$, since changing x would correspond to shifting the singlet field.

With this criteria, solving Eqs. (5) and (6) produces,

$$\mu^2 = \lambda v_{\rm EW}^2, \qquad b_1 = -\frac{v_{\rm EW}^2}{4}a_1. \tag{7}$$

Using these solutions, the potential can be written in a more suggestive form, in terms of the neutral component of the Higgs field:

$$\begin{aligned} V(\phi_0, S) = {} & \lambda\left(\phi_0^2 - \frac{v_{\rm EW}^2}{2}\right)^2 + \frac{a_1}{2}\left(\phi_0^2 - \frac{v_{\rm EW}^2}{2}\right)S \\ & + \frac{a_2}{2}\left(\phi_0^2 - \frac{v_{\rm EW}^2}{2}\right)S^2 + \frac{1}{4}(2b_2 + a_2 v_{\rm EW}^2)S^2 \\ & + \frac{b_3}{3}S^3 + \frac{b_4}{4}S^4, \end{aligned} \tag{8}$$

where an arbitrary constant factor has been dropped. Then $v = v_{\rm EW}$ and $x = 0$ is a minimum by construction.

A. Scalar masses and mixing

The scalar mass matrix is,

$$V_{\rm mass} = \frac{1}{2}UM^2U^T, \tag{9}$$

where

$$U = (\,h \quad S\,), \tag{10}$$

$$M^2 \equiv \begin{pmatrix} M_{11}^2 & M_{12}^2 \\ M_{12}^2 & M_{22}^2 \end{pmatrix} = \begin{pmatrix} 3\lambda v^2 - \mu^2 + x(a_1 + a_2 x)/2 & a_1 v/2 + a_2 v x \\ a_1 v/2 + a_2 v x & b_2 + a_2 v^2/2 + x(2b_3 + 3b_4 x) \end{pmatrix}. \tag{11}$$

The mass eigenstates are

$$\begin{pmatrix} h_1 \\ h_2 \end{pmatrix} = \begin{pmatrix} \cos\theta & \sin\theta \\ -\sin\theta & \cos\theta \end{pmatrix}\begin{pmatrix} h \\ S \end{pmatrix}. \tag{12}$$

The physical masses of h_1 and h_2 are m_1^2 and m_2^2, respectively:

$$m_{1,2}^2 = \frac{1}{2}\left(M_{11}^2 + M_{22}^2 \mp \sqrt{(M_{11}^2 - M_{22}^2)^2 + 4M_{12}^4}\right). \tag{13}$$

Note that the range of the mixing angle is $-\pi/4 < \theta < \pi/4$. We take h_1 to be the SM-like Higgs boson with $m_1 = 126$ GeV.

As mentioned earlier, we are interested in the scenario where $(v,x) = (v_{\rm EW}, 0)$ is the global minimum of the potential. Hence, we require that the correct masses and mixing of the Higgs bosons are reproduced at this minimum:

$$\begin{aligned} \det M^2|_{\substack{v=v_{\rm EW}\\ x=0}} &= m_1^2 m_2^2, \\ {\rm Tr} M^2|_{\substack{v=v_{\rm EW}\\ x=0}} &= m_1^2 + m_2^2, \quad \text{and} \\ \left.\frac{2M_{12}^2}{m_1^2 - m_2^2}\right|_{\substack{v=v_{\rm EW}\\ x=0}} &= \sin 2\theta. \end{aligned} \tag{14}$$

From inspection, using Eq. (7) and $x = 0$, the mass matrix only depends on three combinations of parameters. These can be solved for[2]:

[1]The discussion in this section closely follows that of Ref. [21].

[2]There are two solutions. We choose this solution by using the further constraint that λ obtains the SM value, $\lambda = m_1^2/2v_{\rm EW}^2$, in the limit $\theta \to 0$.

$$
\begin{aligned}
a_1 &= \frac{m_1^2 - m_2^2}{v_{\rm EW}} \sin 2\theta, \\
b_2 + \frac{a_2}{2} v_{\rm EW}^2 &= m_1^2 \sin^2\theta + m_2^2 \cos^2\theta, \\
\lambda &= \frac{m_1^2 \cos^2\theta + m_2^2 \sin^2\theta}{2 v_{\rm EW}^2}. \qquad (15)
\end{aligned}
$$

Our free parameters are then:

$$
\begin{aligned}
m_1 &= 126\ \text{GeV}, m_2, \theta, \\
v_{\rm EW} &= 246\ \text{GeV}, \\
x &= 0, a_2, b_3, b_4. \qquad (16)
\end{aligned}
$$

Note that once we choose the masses, mixing, and vevs, there is little choice in the free parameters. That is, all parameters are fully determined except a_2, b_2, b_3, and b_4, and there is a relation between b_2 and a_2.

Since the singlet Higgs does not couple to the SM fermions and vector bosons, the couplings of h_1 and h_2 are determined by those of the neutral component, h, of the Higgs doublet. From Eq. (12), one can see that the coupling of h_1 to the SM fermions and vector bosons, normalized to the SM values, is suppressed by a factor $\cos\theta$, while the coupling of h_2 is suppressed by $-\sin\theta$.

The self-interactions of the Higgs bosons in the basis of mass eigenstates h_1 and h_2 are

$$
\begin{aligned}
V_{\rm self} \supset & \frac{\lambda_{111}}{3!} h_1^3 + \frac{\lambda_{211}}{2!} h_2 h_1^2 + \frac{\lambda_{221}}{2!} h_2^2 h_1 + \frac{\lambda_{222}}{3!} h_2^3 \\
& + \frac{\lambda_{1111}}{4!} h_1^4 + \frac{\lambda_{2111}}{3!} h_2 h_1^3 + \frac{\lambda_{2211}}{4} h_2^2 h_1^2 \\
& + \frac{\lambda_{2221}}{3!} h_2^3 h_1 + \frac{\lambda_{2222}}{4!} h_2^4. \qquad (17)
\end{aligned}
$$

The cubic and quartic couplings are listed in Appendix A.

The partial width of $h_2 \to h_1 h_1$ is then

$$
\Gamma(h_2 \to h_1 h_1) = \frac{\lambda_{211}^2}{32\pi m_2} \sqrt{1 - \frac{4m_1^2}{m_2^2}}. \qquad (18)
$$

Since the coupling of h_2 to other SM particles is suppressed by $\sin\theta$ we can write the total width[3]

$$
\Gamma(h_2) = \sin^2\theta \Gamma^{\rm SM}|_{m_2} + \Gamma(h_2 \to h_1 h_1), \qquad (19)
$$

where $\Gamma^{\rm SM}|_{m_2}$ is the SM Higgs total width evaluated at mass m_2. In future calculations we use the results in Ref. [32] to calculate $\Gamma^{\rm SM}$.

[3]We neglect the partial width $h_2 \to h_1 h_1 h_1$ since this is additionally suppressed by three body phase space.

B. Vacuum structure

Vacuum stability requires that the scalar potential must be positive definite as ϕ_0 and S become large. The behavior of the potential at large values of the fields is governed by the quartic interactions,

$$
4\lambda\phi_0^4 + 2a_2\phi_0^2 S^2 + b_4 S^4 > 0. \qquad (20)
$$

We know that λ and b_4 must both be positive since the potential needs to be stable along the axes $S = 0$ or $\phi_0 = 0$. Also, for $a_2 > 0$ the potential is clearly stable. For $a_2 < 0$, rewrite Eq. (20) as,

$$
\lambda\left(2\phi_0^2 + \frac{a_2}{2\lambda} S^2\right)^2 + \left(b_4 - \frac{a_2^2}{4\lambda}\right) S^4 > 0. \qquad (21)
$$

Since the first term is positive definite, we obtain the stability bound

$$
-2\sqrt{\lambda b_4} \le a_2. \qquad (22)
$$

Following the methods of Ref. [21], the extrema of Eq. (8) for which $v \neq 0$ can be found:

$$
(v, x) = (v_{\rm EW}, 0), \quad \text{and} \quad (v, x) = (v_\pm, x_\pm) \qquad (23)
$$

where

$$
\begin{aligned}
x_\pm &\equiv \frac{v_{\rm EW}(3a_1 a_2 - 8b_3\lambda) \pm 8\sqrt{\Delta}}{4v_{\rm EW}(4b_4\lambda - a_2^2)} \\
v_\pm^2 &\equiv v_{\rm EW}^2 - \frac{1}{2\lambda}(a_1 x_\pm + a_2 x_\pm^2), \\
\Delta &= \frac{v_{\rm EW}^2}{64}(8b_3\lambda - 3a_1 a_2)^2 - \frac{m_1^2 m_2^2}{2}(4b_4\lambda - a_2^2). \qquad (24)
\end{aligned}
$$

For three real solutions to exist, we need $\Delta > 0$ and $v_\pm^2 > 0$. There are also solutions for $v = 0$, which we include in the appendix.

First, we analyze the $v^2 \neq 0$ solutions. For the global minimum to be $v = v_{\rm EW}$ and $x = 0$, the potential of Eq. (8) must satisfy

$$
V(v_{\rm EW}, 0) < V(v_\pm, x_\pm). \qquad (25)
$$

It can be shown that this occurs for

$$
\begin{aligned}
& v_{\rm EW}|8\lambda b_3 - 3a_1 a_2| < 6 m_1 m_2 \sqrt{4b_4\lambda - a_2^2}, \quad \text{or} \\
& 4b_4\lambda < a_2^2. \qquad (26)
\end{aligned}
$$

The vacuum structure of $v^2 \neq 0$ is shown in Fig. 1 with $m_2 = 370$ GeV, $\cos\theta = \sqrt{0.88}$, and $b_4 = 1$. The region with $a_2 \lesssim -1$ does not satisfy the stability bound of Eq. (22). The white region is where the $(v, x) = (v_{\rm EW}, 0)$ solution is

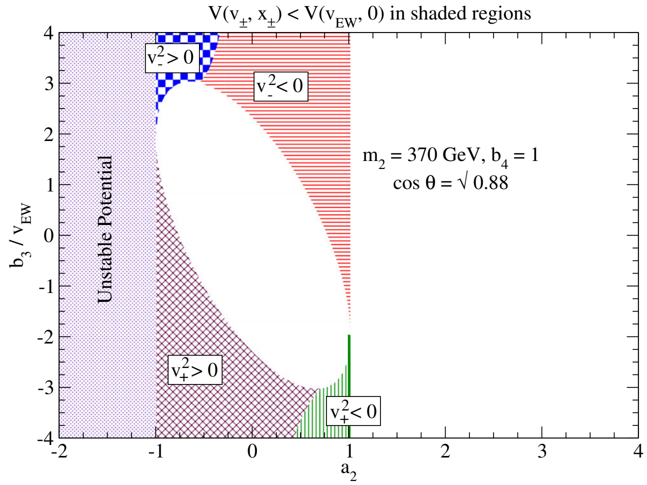

FIG. 1 (color online). Structure of the $v^2 \neq 0$ vacua in the b_3 vs a_2 plane for $m_2 = 370$ GeV, $b_4 = 1$, and $\cos\theta = \sqrt{0.88}$. The different regions are where the $(v, x) = (v_{\rm EW}, 0)$ minimum is the lowest lying (white region), (v_-, x_-) is the lowest lying minimum with $v_-^2 < 0$ (red horizontal lines) and $v_-^2 > 0$ (blue squares), and (v_+, x_+) is the lowest lying minimum with $v_+^2 < 0$ (green vertical lines), and $v_+^2 > 0$ (maroon hatched region).

the lowest lying minimum with $v^2 \neq 0$, as given in Eq. (26). The shaded areas show b_3, a_2 values where $V(v_-, x_-) < V(v_{\rm EW}, 0)$ with $v_-^2 < 0$ (red horizontal lines) and $v_-^2 > 0$ (blue squares), and $V(v_+, x_+) < V(v_{\rm EW}, 0)$ with $v_+^2 < 0$ (green vertical lines) and $v_+^2 > 0$ (maroon hatched lines). All three solutions are never simultaneously minima.

It can be shown that $(v_{\rm EW}, 0)$ always corresponds to a minimum. Hence, this exhausts the possibilities for $v^2 \neq 0$. Since we require that the global minimum be real, we can also reject solutions for which $v_\pm^2 < 0$. Hence, $v = v_{\rm EW}$ and $x = 0$ is the lowest lying real minimum with $v^2 \neq 0$ in the red-lined, green-lined, and white regions. However, we must consider also the case $v = 0$, which is discussed in the appendix.

The final results for the allowed (b_3, a_2) region with a global minimum at $(v, x) = (v_{\rm EW}, 0)$ are shown in Fig. 2. This includes the analysis of the $v = 0$ minima. Inside the contours $(v, x) = (v_{\rm EW}, 0)$ is the global minimum. Figure 2(a) shows the dependence on the heavy scalar mass m_2, and Fig. 2(b) shows the dependence on b_4. Increasing b_4 and m_2 increases the upper bounds on a_2 slightly. The difference in allowed regions between Figs. 1 and 2(a) corresponds to the case where the $v = 0$ minimum is the global minimum.

In Fig. 2(a), there is an interesting point on the contours that appears to be independent of m_2. From Eq. (26), this section of the contour arises from the inequality

$$b_3^{\rm min} \equiv \frac{3}{8\lambda v_{\rm EW}}\left(a_1 a_2 v_{\rm EW} - 2m_1 m_2\sqrt{4b_4\lambda - a_2^2}\right) < b_3. \tag{27}$$

The stationary points on this line can be found by solving $\partial b_3^{\rm min}/\partial m_2 = 0$ for a_2. Assuming $\sin\theta > 0$, one of these solutions corresponds to

$$a_2 = -\sqrt{2b_4}\cos\theta\frac{m_1}{v_{\rm EW}}, \quad \text{and} \quad b_3 = -\frac{3}{2}\sqrt{2b_4}\sin\theta m_1, \tag{28}$$

which is independent of m_2. This exactly corresponds to the degenerate point on the contours in Fig. 2(a).

It is clear from these results that both a_2 and b_3 are bounded for fixed masses, mixing, and b_4. As we will see in Sec. IV, requiring perturbative unitarity bounds b_4. Hence, all parameters are either determined by the masses and

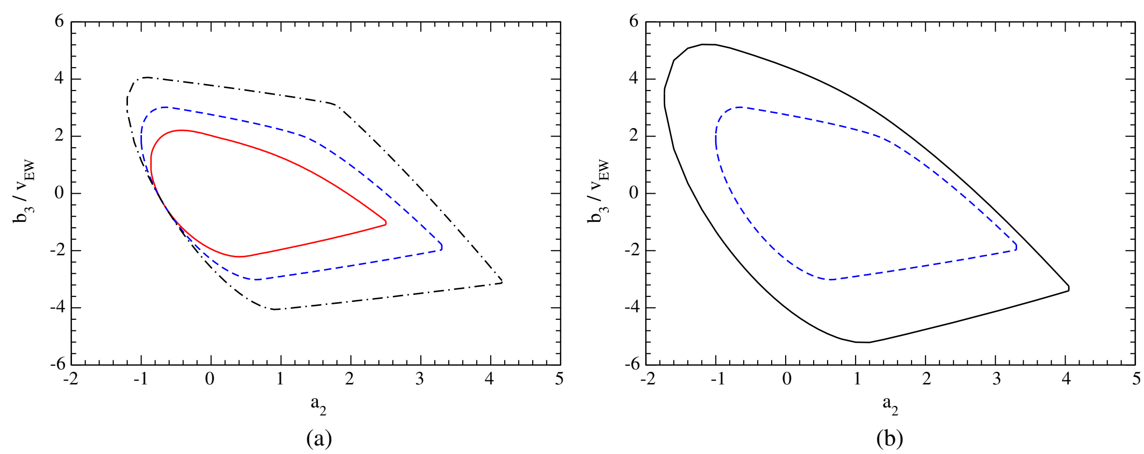

FIG. 2 (color online). Constraints on the (b_3, a_2) parameter space obtained by requiring that the global minimum is at $(v, x) = (v_{\rm EW} = 246\ {\rm GeV}, 0)$. Regions enclosed by the lines are allowed. Figure 2(a) shows the allowed regions with various values of m_2 for $b_4 = 1$. The solid (red), dashed (blue), and dash-dotted (black) represent $m_2 = 270$, 370, and 500 GeV, respectively. Figure 2(b) shows the allowed regions with $b_4 = 1$ (blue dashed) and $b_4 = 3$ (black solid) for $m_2 = 370$ GeV. The parameters used are $m_1 = 126$ GeV and $\cos\theta = 0.94$.

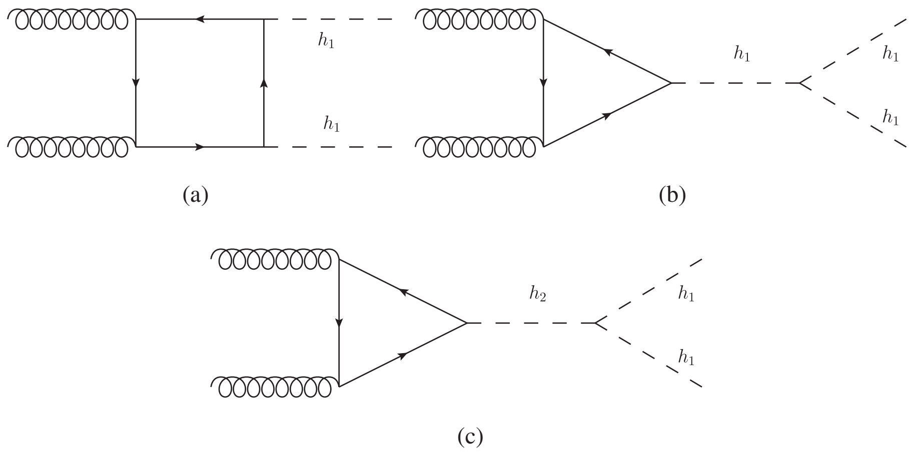

FIG. 3. Representative diagrams for di-Higgs production corresponding to (a) box diagram, (b) triangle diagram exchanging the light Higgs h_1, and (c) triangle diagram exchanging the heavy Higgs h_2. The solid lines stand for fermions, where top quark loops give the dominant contributions.

mixings of the Higgs sector or are bounded by theoretical considerations. This will have a direct influence on the phenomenology of the singlet model at the LHC.

III. RESONANT DI-HIGGS PRODUCTION

A. Results without a Z_2 symmetry

We turn now to the results for di-Higgs production obtained by imposing the parameter restrictions described above to find the maximum enhancement possible in the $gg \to h_1 h_1$ channel relative to the SM rate. Di-Higgs production proceeds through the diagrams shown in Fig. 3. For $m_2 \gtrsim 2m_1$, it is possible to have a large resonant enhancement from the diagram of Fig. 3(c). Our numerical results use CT12NLO PDFs with $\mu = M_{h_1 h_1}$. We normalize many of our plots to the LO SM predictions, $\sigma(gg \to h_1 h_1)|_{\rm SM} = 15$ fb (0.6 pb) at $\sqrt{S} = 14$ TeV (100 TeV).[4]

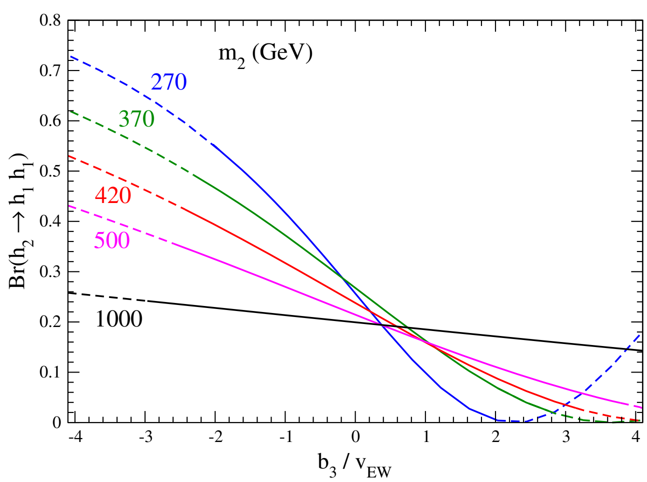

FIG. 4 (color online). The branching ratio of $h_2 \to h_1 h_1$ as a function of b_3. The parameters used are $m_1 = 126$ GeV, $\cos\theta = 0.94$, $a_2 = 0$, $v_{\rm EW} = 246$ GeV, and $b_4 = 1$. Lines from top to bottom are $m_2 = 270, 370, 420, 500$, and 1000 GeV. The solid (dashed) lines stand for regions that are allowed (excluded) by the requirement of EW stability.

From the mass matrix in Eq. (11), we know that varying b_3 does not change m_1, m_2 and the mixing angle θ. In contrast, one can observe that λ_{211} in Eq. (A1) is a function of b_3. In Fig. 4, we show the dependence on b_3 of the branching ratio of the heavier Higgs, h_2, into the SM-like Higgs, h_1. For b_3 small, the branching ratio has little dependence on m_2, while for large b_3, the branching ratio can be large and depends significantly on b_3. The dotted curves represent regions where the parameters do not correspond to a global electroweak minimum. We see then that for a given mass this constraint corresponds to an upper limit on the branching ratio ${\rm Br}(h_2 \to h_1 h_1)$.

To understand the features of Fig. 4, use the solutions in Eq. (15) to rewrite

$$\lambda_{211} = \sin\theta\left[-\frac{2m_1^2 + m_2^2}{v_{\rm EW}}\cos^2\theta - a_2 v_{\rm EW}(1 - 3\cos^2\theta) + b_3 \sin(2\theta)\right]. \quad (29)$$

From this we see that $b_3 \sin(2\theta)$ and m_2 make opposite sign contributions to λ_{211}. Hence, for $b_3 \sin(2\theta) < 0$, they constructively contribute to λ_{211}. The major feature of this region in Fig. 4 is then understood by noting that the partial widths of h_2 into h_1, Ws, and Zs scale like

$$\Gamma(h_2 \to h_1 h_1) \propto \sin^2\theta m_2, \quad \text{and}$$
$$\Gamma(h_2 \to W^+W^-/ZZ) \propto \sin^2\theta m_2^3. \quad (30)$$

[4]Radiative corrections in the SM are large, typically a factor of ~ 2 enhancement [7–9], and are not included here since they are simply an overall normalization factor to the results we present.

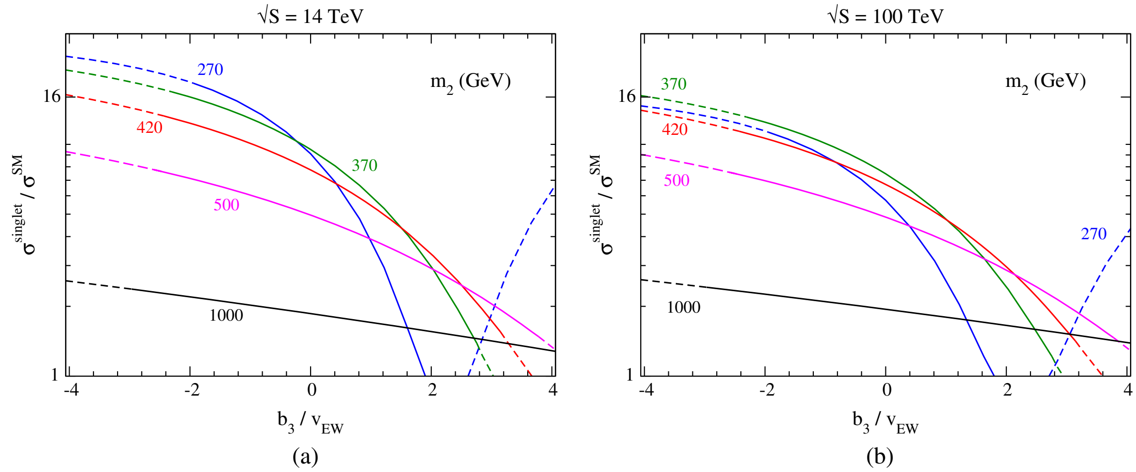

FIG. 5 (color online). The ratio of the di-Higgs cross section in the singlet model to that in the SM at (a) $\sqrt{S} = 14$ TeV and (b) $\sqrt{S} = 100$ TeV as a function of b_3. The parameters used are $m_1 = 126$ GeV, $\cos\theta = 0.94$, $a_2 = 0$, $v_{\mathrm{EW}} = 246$ GeV, and $b_4 = 1$. The solid (dashed) lines stand for regions that are allowed (excluded) by the requirement of EW stability.

Hence, as the mass of h_2 increases the partial widths into Ws and Zs grow much more quickly than the partial width into h_1h_1. The branching ratio $\mathrm{Br}(h_2 \to h_1h_1)$ therefore decreases with mass.

The region for $b_3 \sin(2\theta) > 0$ is slightly more involved. Using Eq. (29), the triple coupling λ_{211} goes to zero when

$$b_3 \sin(2\theta) = \frac{2m_1^2 + m_2^2}{v_{\mathrm{EW}}}\cos^2\theta + a_2 v_{\mathrm{EW}}(1 - 3\cos^2\theta). \tag{31}$$

We see that for smaller m_2 the zero corresponds to smaller $b_3 \sin(2\theta)$. As $b_3 \sin(2\theta)$ goes from negative to positive, the smaller m_2 values turn over and approach zero more quickly than the larger m_2. This is the behavior we see in Fig. 4. Note that for our representative parameters, we have $\theta > 0$, so the sign of $b_3 \sin(2\theta)$ is the same as b_3.

In Fig. 5, we plot the dependence of the ratio of the di-Higgs production cross section in the singlet model to that in the SM. In this type of model, the double Higgs production cross section can reach up to $\mathcal{O}(10)$ times that of the SM with $58\% \gtrsim \mathrm{Br}(h_2 \to h_1h_1) \gtrsim 28\%$. Interestingly, the enhancement does not grow as $\sqrt{S}$ is increased from 14 TeV to 100 TeV, although of course the total rate is increased. Both the SM and singlet rates are dominated by gluon fusion production; hence, both rates are similarly increased between 14 and 100 TeV.

The di-Higgs enhancement depends on the production cross section of h_2 and the branching ratio of $h_2 \to h_1h_1$. Since the production cross section of lower mass states is generically larger than that of high mass states, $m_2 = 270$ GeV has the largest enhancement for $b_3 < 0$. For $b_3 > 0$, it is possible for the branching ratio of $h_2 \to h_1h_1$ to go to zero. The behavior of the enhancement in this region closely follows the discussion of Fig. 4. For $\sqrt{S} = 100$ TeV and $b_3 < 0$ [Fig. 5(b)], the cross section for $m_2 = 270$ GeV drops below that of $m_2 = 370$ GeV. As to be discussed later, this is due to specific properties of di-Higgs production.

In Fig. 6 we show the enhanced di-Higgs ratio as a function of the $h_2 \to h_1h_1$ branching ratio. If the narrow width approximation holds and the production cross section h_2 is sufficiently larger than the SM di-Higgs rate, we have

$$\sigma(pp \to h_1h_1) \approx \sigma(pp \to h_2)\mathrm{Br}(h_2 \to h_1h_1). \tag{32}$$

Hence, we would expect this dependence to be a straight line, as seen for $m_2 = 270$ and 420 GeV. However, we see that this is not the case for $m_2 = 1000$ GeV. In Fig. 7 we show the ratio of the total width of h_2 and m_2 as a function of the branching ratio of $h_2 \to h_1h_1$. As can be seen for $m_2 = 1000$ GeV, the width is always large and the narrow width approximation is poor. This explains why the $m_2 = 1000$ GeV line in Fig. 6 is not straight. Also, as the branching ratio of $h_2 \to h_1h_1$ increases, the total width become larger. This is due to the partial width $h_2 \to h_1h_1$ becoming large, since the partial widths into W and Z boson is fixed by the mass m_2 and mixing angle θ.

In Fig. 6, it is interesting to note that the enhancement for $m_2 = 420$ GeV is larger than that for 270 GeV at $\sqrt{S} = 100$ TeV. This can be understood from the parton luminosity plot of Fig. 8(a), where we show the gluon-gluon parton luminosity (normalized to that at $2m_t$). The $\sqrt{S} = 14$ TeV luminosity falls much more quickly as a function of invariant mass than does the corresponding luminosity at $\sqrt{S} = 100$ TeV. We compare this with the resonant production of $gg \to h_2$ in Fig. 8(b) and observe that at $\sqrt{S} = 100$ TeV the resonant enhancement at the $t\bar{t}$ threshold is more important than at $\sqrt{S} = 14$ TeV. Finally,

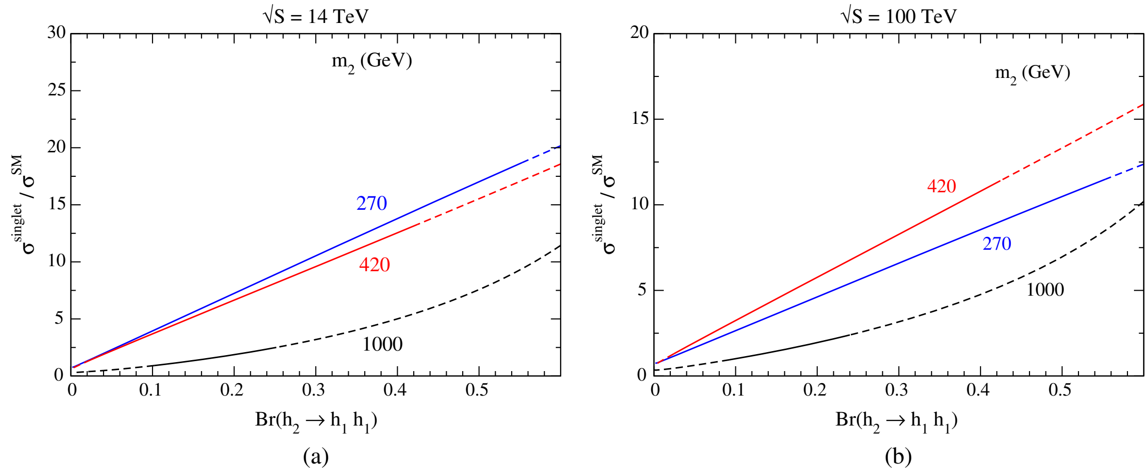

FIG. 6 (color online). The ratio of the di-Higgs cross section in the singlet model to that in the SM at (a) $\sqrt{S} = 14$ TeV and (b) $\sqrt{S} = 100$ TeV as a function of the branching ratio of $h_2 \to h_1 h_1$. The parameters used are $m_1 = 126$ GeV, $\cos\theta = 0.94$, $a_2 = 0$, $v_{\mathrm{EW}} = 246$ GeV, and $b_4 = 1$. The solid (dashed) lines stand for regions that are allowed (excluded) by the requirement of EW stability. $m_2 = 270$ (brown), 420 (red), and 1000 GeV (black), respectively.

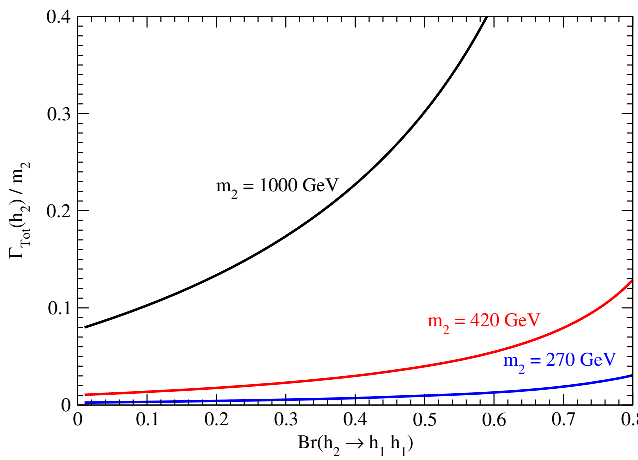

FIG. 7 (color online). The total width of h_2 as a ratio with m_2 vs the branching ratio $h_2 \to h_1 h_1$. The parameters used are $m_1 = 126$ GeV, $\cos\theta = 0.94$, $a_2 = 0$, $v_{\mathrm{EW}} = 246$ GeV, and $b_4 = 1$. The masses are $m_2 = 270$ GeV (blue), 420 GeV (red), and 1000 GeV (black).

we show the dependence on m_2 of the full cross section for $gg \to h_1 h_1$ in Fig. 9. The resonant structure near $2m_t$ is clearly visible.

B. The Z_2 limit

It may be necessary in certain models to impose a Z_2 symmetry on the potential under which S is odd and H is even. This may be motivated from a dark matter perspective, where S is a dark matter particle, or the point of view of a complex hidden sector. The potential for this case can be obtained in the limit $a_1, b_1, b_3 \to 0$. If the Z_2 remains unbroken, there is no resonance enhancement in di-Higgs production, since the $S \to hh$ decay breaks the Z_2 symmetry and there is no mixing between S and h. We ignore this case. However, the Z_2 symmetry may be broken by a vev of S. Unlike the case outlined above, the vev of S is then physically meaningful and we cannot set $\langle S \rangle = x = 0$ arbitrarily. The Z_2 symmetric potential is

$$V(H,S) = -\mu^2 H^\dagger H + \lambda (H^\dagger H)^2 + \frac{a_2}{2} H^\dagger H S^2 + \frac{b_2}{2} S^2 + \frac{b_4}{4} S^4. \tag{33}$$

We shift the fields in the usual manner to find the $h_2 h_1 h_1$ coupling in the Z_2 symmetric limit [10],

$$\lambda_{211}^{Z_2} = a_2 [vs(2c^2 - s^2) - xc(2s^2 - c^2)] - 6\lambda v c^2 s + 6 b_4 x c s^2. \tag{34}$$

In the limit $x = 0$ and a_1, b_1, and $b_3 = 0$, Eq. (34) is in agreement with Eq. (A1). We impose the conditions of positivity of the potential, $\lambda > 0$, $b_4 > 0$ and $4\lambda b_4 - a_2^2 > 0$ [Eq. (20)] and require the couplings to be perturbative, $a_2, b_4, \lambda < 4\pi$.

The physical parameters are taken as

$$m_1, m_2, \cos\theta \equiv c, v_{\mathrm{EW}}, x. \tag{35}$$

Using Eqs. (34) and (18), the branching ratio for $h_2 \to h_1 h_1$ can be found and is shown in Fig. 10. Comparing with Fig. 6, it is apparent that the branching ratios are similar in the models with and without the Z_2 symmetry for large values of x/v_{EW}, where the branching ratio asymptotes to around $\mathrm{BR}(h_2 \to h_1 h_1) \sim 0.3$. The branching ratio $h_2 \to h_1 h_1$ appears to have little discriminating power between the Z_2 symmetric and nonsymmetric potentials.

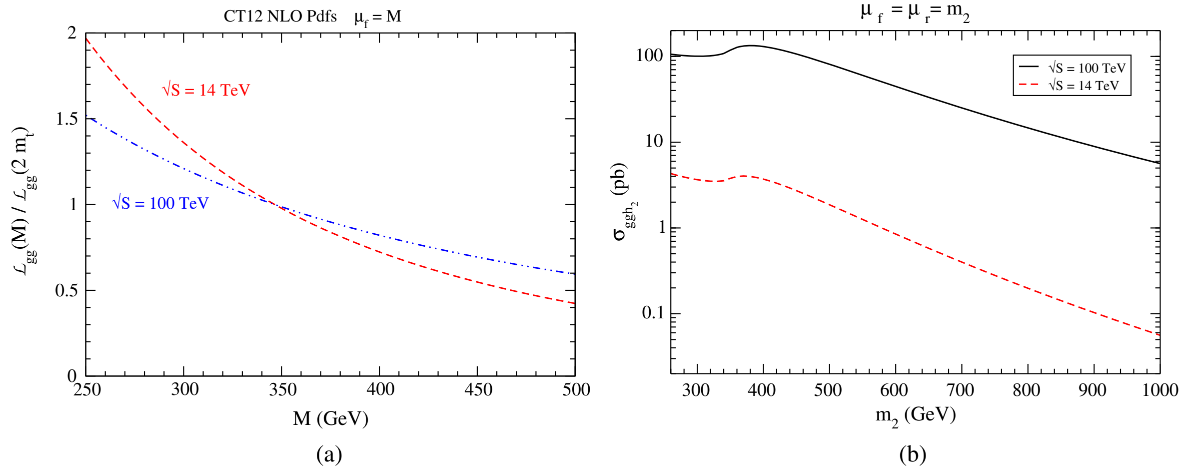

FIG. 8 (color online). (a) Gluon gluon luminosity at $\sqrt{S} = 14$ and 100 TeV as a function of invariant mass, M. (b) Resonant contribution from $gg \to h_2$, evaluated at a scale, $\mu = m_2$ with $\cos\theta = .94$.

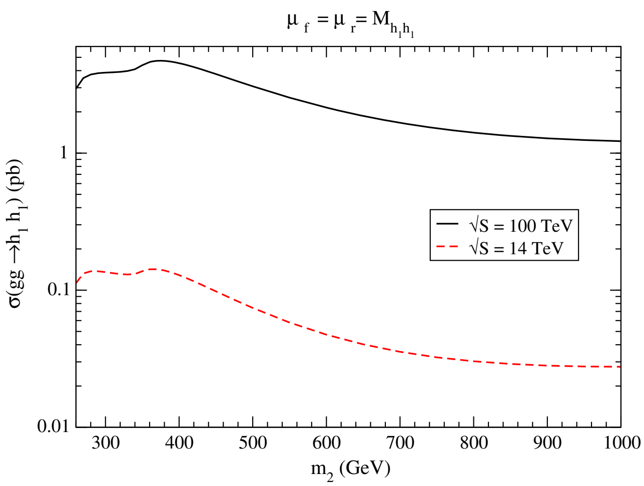

FIG. 9 (color online). Total cross section for $gg \to h_1 h_1$ as a function of m_2 for $b_3 = a_2 = 0$, $b_4 = 1$, and $\cos\theta = .94$.

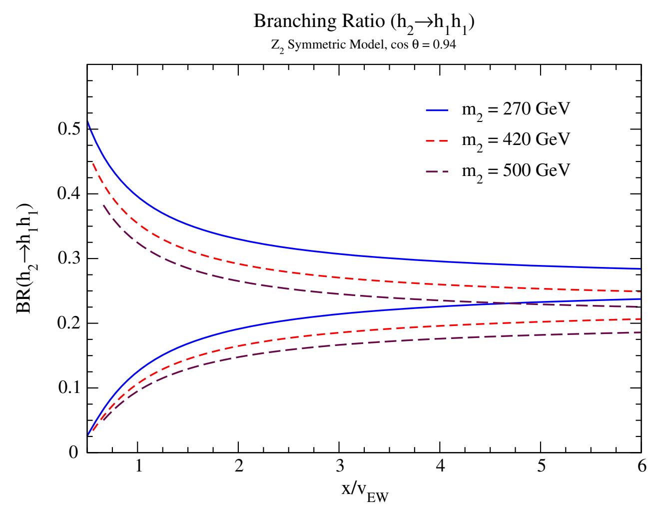

FIG. 10 (color online). The branching ratio of $h_2 \to h_1 h_1$ in a Z_2 symmetric model as a function of the vev of the singlet field, x. The upper (lower) branches of the curves correspond to negative (positive) values of $\sin\theta$.

IV. EXPERIMENTAL AND THEORETICAL CONSTRAINTS

There are a number of well-known experimental and theoretical limits on the Higgs singlet model, which we briefly review in this section.

A. Experimental limits

From the direct measurements of the Higgs coupling strengths, ATLAS [33] places a constraint on the mixing angle, θ, of the singlet model, where $\cos^2\theta \le 0.88$ has been excluded at 95% CL. This limit assumes that there is no branching ratio to invisible particles. Here we take the upper limit of $\sin^2\theta \le 0.12$ as a representative point. Direct searches for the heavy Higgs (h_2) decaying into W^+W^- and ZZ from ATLAS and CMS [34,35] can also give bounds on $\sin^2\theta$ with $\sin^2\theta \lesssim 0.2$ for $m_2 \sim 200$–400 GeV and $\sin^2\theta \lesssim 0.4$ for $m_2 \sim 600$ GeV. However, these constraints are not as strong as the ATLAS limit from the Higgs coupling strengths.

The existence of a Higgs singlet which mixes with the SM Higgs boson is also restricted by electroweak precision observables. A fit to the oblique parameters, S and T (fixing U to be 0), is shown in Fig. 11 [20,36]. We see that limits from the oblique parameters are not competitive with the ATLAS limit from the Higgs coupling strengths.

ATLAS and CMS have obtained upper bounds on the cross section for the resonant production of SM Higgs bosons pairs through the process $pp \to h_2^* \to h_1 h_1$ in the $\gamma\gamma b\bar{b}$ [37,38] and $b\bar{b}b\bar{b}$ [39] channels at a center-of-mass energy of $\sqrt{S} = 8$ TeV with an integrated luminosity of 20 fb^{-1} as summarized in Fig. 12. In the low mass region the $\gamma\gamma b\bar{b}$ channel gives a stronger bound as opposed to a weaker bound obtained in the $b\bar{b}b\bar{b}$ channel due to the

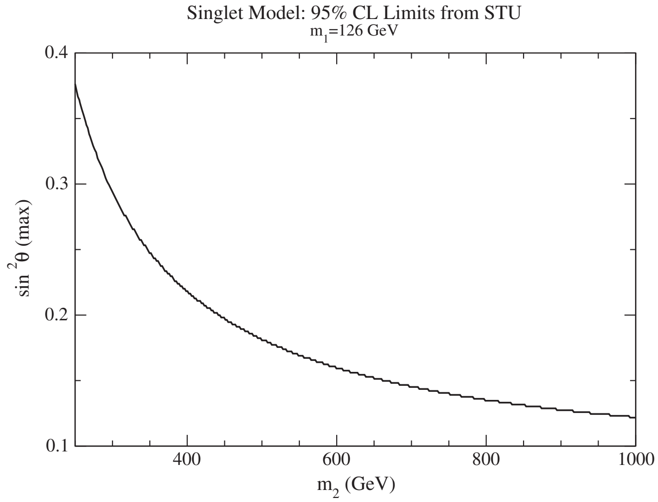

FIG. 11. Constraints on the mixing angle, $\sin\theta$, as a function of the mass of the heavier Higgs scalar, m_2, from fits to the oblique parameters, S and T.

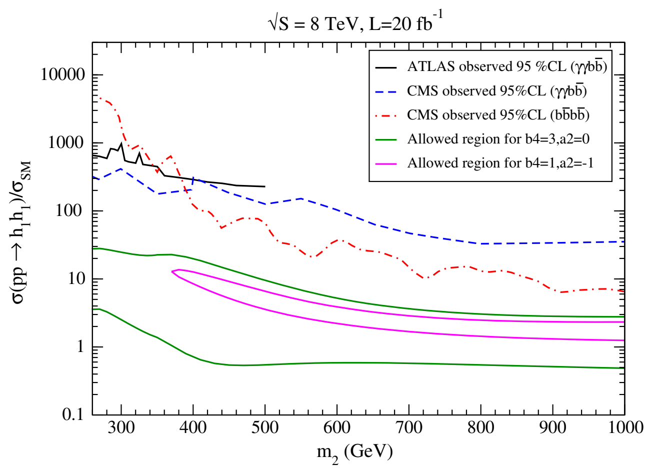

FIG. 12 (color online). Observed 95% CL upper limits at $\sqrt{S} = 8$ TeV with an integrated luminosity of 20 fb^{-1} on the resonant di-Higgs production cross section from ATLAS in the $\gamma\gamma b\bar{b}$ channel (black solid), CMS in the $\gamma\gamma b\bar{b}$ channel (blue dashed) and CMS in the $b\bar{b}b\bar{b}$ channel (red dot-dashed), normalized to the leading order cross section predicted by the SM, and the regions allowed by the requirement that the electroweak minimum be a global minimum for $(b_4, a_2) = (3, 0)$ (green solid) and $(b_4, a_2) = (1, -1)$ (magenta solid).

large QCD background. However, the limit from the $b\bar{b}b\bar{b}$ channel becomes more constraining above $m_2 \sim 400$ GeV.

We compare the experimental upper limits on the production cross sections for resonant di-Higgs production with m_2 between 270 GeV and 1 TeV, normalized to the leading order cross section predicted by the SM, with the range of allowed cross sections consistent with the requirement that the parameters correspond to a global electroweak minimum. (The allowed region is between the curves). Two sets of parameter points $(b_4, a_2) = (3, 0)$ and $(b_4, a_2) = (1, -1)$ are considered. The former has a larger value of b_4 and hence the bound is less stringent as illustrated in Fig. 2(b). The lower limit of the allowed region on m_2, which starts at $m_2 \sim 370$ GeV, for $(b_4, a_2) = (1, -1)$ can be explained by Eq. (22) as due to the vacuum stability constraint. Plugging in λ defined in Eq. (15), one can obtain the lower limit for m_2^2 for a given b_4 and negative a_2,

$$m_2^2 \geq \frac{1}{\sin^2\theta}\left(\frac{a_2^2}{2b_4}v_{\mathrm{EW}}^2 - m_1^2\cos^2\theta\right). \tag{36}$$

Throughout the $m_2 < 1$ TeV mass range, the constraints derived from the global electroweak minimum requirement are always stronger than those currently available from the LHC experiments at $\sqrt{S} = 8$ TeV. We make naive projections for the expected constraints at the LHC at $\sqrt{S} = 14$ TeV with an integrated luminosity of 300 fb^{-1} by rescaling the expected 95% CL upper limits at $\sqrt{S} = 8$ TeV with an integrated luminosity of 20 fb^{-1}, using the ratios of gluon-gluon luminosities (evaluated at the scale $2m_1$) given in Ref. [40]. As shown in Fig. 13, the projected bounds from the CMS $\gamma\gamma b\bar{b}$ channel can rule out the entire parameter space where the electroweak minimum is a global minimum for $(b_4, a_2) = (1, -1)$ and can exclude much of the allowed region for $(b_4, a_2) = (3, 0)$. Moreover, the projected limits from the CMS $b\bar{b}b\bar{b}$ channel can potentially exclude the entire parameter space allowed by the electroweak minimum requirement for $(b_4, a_2) = (1, -1)$ and rule out two thirds of the allowed region in the high mass range for $(b_4, a_2) = (3, 0)$.

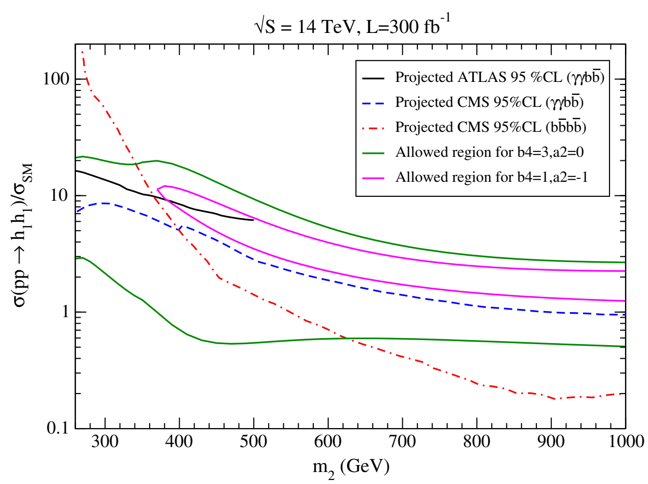

FIG. 13 (color online). Projected 95% CL upper limits at $\sqrt{S} = 14$ TeV with an integrated luminosity of 300 fb^{-1} on the production cross section from the ATLAS $\gamma\gamma b\bar{b}$ channel (black solid), CMS $\gamma\gamma b\bar{b}$ (blue dashed) and CMS $b\bar{b}b\bar{b}$ (red dot-dashed), normalized to the leading order cross section predicted by the SM, and the regions allowed by the requirement that the electroweak minimum be a global minimum for $(b_4, a_2) = (3, 0)$ (green solid) and $(b_4, a_2) = (1, -1)$ (magenta solid).

B. Unitarity

The coefficients of the potential cannot be too large or perturbative unitarity will be violated in the h_ih_j scattering processes [41]. The simplest limit comes from the high energy scattering of $h_2h_2 \to h_2h_2$, where the $J = 0$ partial wave is

$$a_0(h_2h_2 \to h_2h_2) \to_{s \gg m_2^2} \frac{3b_4}{8\pi}. \tag{37}$$

Requiring $|a_0| < \frac{1}{2}$ yields $|b_4| \le 4.2$. Limits from a coupled channel analysis of h_ih_j scattering show that for small $\sin\theta$, multi-TeV scale masses are allowed for m_2 [10].

Similarly, we can consider the $h_1h_1 \to h_1h_1$ scattering to find the $J = 0$ partial wave.

$$a_0(h_1h_1 \to h_1h_1) \to_{s \gg m_1^2} \frac{3\lambda}{8\pi}. \tag{38}$$

Then using Eq. (15) and $|a_0| < \frac{1}{2}$, an upper limit on m_2 can be found:

$$m_2^2 < \frac{1}{3\sin^2\theta}(8\pi v_{\mathrm{EW}}^2 - 3m_1^2\cos^2\theta). \tag{39}$$

For $\cos^2\theta = 0.88$ and $m_1 = 126$ GeV, this limit is $m_2 \lesssim 2$ TeV.

V. DISCUSSION AND CONCLUSIONS

We studied resonance enhancement of di-Higgs production in a generic singlet extended Standard Model. By imposing conditions on the masses, mixing, and vacuum expectation values of the bosons we were able to identify the three parameters that are left free. These three parameters were then bounded by unitarity constraints and the requirement that the electroweak symmetry breaking minimum be the global minimum. With these constraints, $\mathrm{Br}(h_2 \to h_1h_1)$ is bounded from above. Hence, we found that theoretical considerations bound the di-Higgs production in this model and that the theoretical constraints are more stringent than the current limits from direct searches for h_1h_1. We then provided predictions for the cross sections and branching ratios for $\sigma(pp \to h_2 \to h_1h_1)$ at both the 14 TeV LHC and a 100 TeV collider. The di-Higgs production enhancement can be as large as a factor of $\sim 18(13)$ for $m_2 = 270(420)$ GeV relative to the SM rate at 14 TeV for parameters corresponding to a global EW minimum.

ACKNOWLEDGMENTS

This work is supported by the U.S. Department of Energy under Grant No. DE-AC02-98CH10886 and Contract No. DE-AC02-76SF00515.

APPENDIX A: CUBIC AND QUARTIC COUPLINGS

The cubic and quartic couplings in Eq. (17) are listed below,

$$\begin{aligned}
\lambda_{111} &= 2s^3b_3 + \frac{3a_1}{2}sc^2 + 3a_2s^2cv + 6c^3\lambda v,\\
\lambda_{211} &= 2s^2cb_3 + \frac{a_1}{2}c(c^2 - 2s^2) + (2c^2 - s^2)sva_2 - 6\lambda sc^2v\\
\lambda_{221} &= 2c^2sb_3 + \frac{a_1}{2}s(s^2 - 2c^2) - (2s^2 - c^2)cva_2 + 6\lambda cs^2v\\
\lambda_{222} &= 2c^3b_3 + \frac{3a_1}{2}cs^2 - 3a_2c^2sv - 6s^3\lambda v,\\
\lambda_{1111} &= 6(\lambda c^4 + a_2s^2c^2 + b_4s^4)\\
\lambda_{2111} &= 6sc\left(b_4s^2 + \frac{a_2}{2}(1 - 2s^2) - \lambda c^2\right)\\
\lambda_{2211} &= 6s^2c^2(-a_2 + b_4 + \lambda) + a_2\\
\lambda_{2221} &= 6sc\left(b_4c^2 + \frac{a_2}{2}(1 - 2c^2) - \lambda s^2\right)\\
\lambda_{2222} &= 6(s^2c^2a_2 + c^4b_4 + \lambda s^4),
\end{aligned} \tag{A1}$$

and we abbreviate $s = \sin\theta$, $c = \cos\theta$. We assume $\sin\theta > 0$. Flipping the sign of $\sin\theta$ is equivalent to reversing the sign of b_3, as is apparent in Eq. (A1). Note that several couplings are related by a transformation $c \to -s$ and $s \to c$. To understand this, one can see that Eq. (12) is invariant under $c \to -s$, $s \to c$, $h_1 \to h_2$, and $h_2 \to -h_1$. This implies Eq. (17) is also invariant under such transformations. As a result, the couplings $\lambda_{111}, \lambda_{221}, \lambda_{1111}$, and λ_{2222} are transformed into $\lambda_{222}, \lambda_{211}, \lambda_{2222}$, and λ_{1111}, respectively after the replacement $c \to -s$ and $s \to c$ while λ_{2211} remains invariant. Similarly, $\lambda_{211}, \lambda_{222}, \lambda_{2111}$, and λ_{2221} are transformed into $\lambda_{221}, \lambda_{111}, \lambda_{2221}$, and λ_{2111}, respectively under $c \to -s$ and $s \to c$ up to a minus sign because they are associated with odd numbers of h_2. In the small angle limit, to $\mathcal{O}(s^2)$,

$$\begin{aligned}
\lambda_{111} &\to 6\lambda v + \frac{3}{2}a_1s + 3vs^2(a_2 - 3\lambda)\\
\lambda_{211} &\to \frac{a_1}{2} + sv(-6\lambda + 2a_2) + \frac{s^2}{4}(8b_3 - 7a_1)\\
\lambda_{221} &\to 2sb_3 - a_1s + \left(1 - \frac{7}{2}s^2\right)va_2 + 6\lambda s^2v\\
\lambda_{222} &\to (2 - 3s^2)b_3 + \frac{3a_1}{2}s^2 - 3a_2sv,\\
\lambda_{1111} &\to 6\lambda - 6s^2(2\lambda - a_2)\\
\lambda_{2111} &\to 3s(a_2 - 2\lambda)\\
\lambda_{2211} &\to a_2 + 6s^2(-a_2 + b_4 + \lambda)\\
\lambda_{2221} &\to 3s(2b_4 - a_2)\\
\lambda_{2222} &\to 6b_4 + 6s^2(a_2 - 2b_4).
\end{aligned} \tag{A2}$$

APPENDIX B: $v = 0$ SOLUTIONS

We now evaluate the extrema of the potential with $v = 0$. These are found by evaluating the extrema of Eq. (8). The solutions for $\langle S\rangle$ are

$$x_1^0 = \frac{(2b_3 - \kappa^{1/3})^2 - 12b_2b_4}{6b_4\kappa^{1/3}} + \frac{b_3}{3b_4}$$
$$x_2^0 = \frac{(2b_3 - e^{2i\pi/3}\kappa^{1/3})^2 - 12b_2b_4}{6b_4e^{2i\pi/3}\kappa^{1/3}} + \frac{b_3}{3b_4}$$
$$x_3^0 = \frac{(2b_3 - e^{4i\pi/3}\kappa^{1/3})^2 - 12b_2b_4}{6b_4e^{4i\pi/3}\kappa^{1/3}} + \frac{b_3}{3b_4}, \qquad \text{(B1)}$$

where we have defined,

$$\kappa = -4b_3(2b_3^2 - 9b_2b_4) + 27a_1b_4^2v_{\mathrm{EW}}^2 + 3b_4\sqrt{3\Delta^0}$$
$$\Delta^0 = -16b_2^2(b_3^2 - 4b_2b_4) - 8a_1b_3v_{\mathrm{EW}}^2(2b_3^2 - 9b_2b_4) + 27a_1^2b_4^2{v_{\mathrm{EW}}}^4. \qquad \text{(B2)}$$

In Fig. 14, we show the vacuum structure of the $\langle\phi_0\rangle = 0$ minima compared to the $(v, x) = (v_{\mathrm{EW}}, 0)$ minima. The white region corresponds to where the EWSB minima lies below the $v = 0$ minima, the red lined region to where $(v, x) = (0, x_1^0)$ lies below $(v_{\mathrm{EW}}, 0)$, the blue squares to where $(0, x_2^0)$ lies below $(v_{\mathrm{EW}}, 0)$, and the green hashed region is where both $(0, x_1^0)$ and $(0, x_2^0)$ lie below $(v_{\mathrm{EW}}, 0)$. We do not find any region where $V(0, \langle S\rangle = x_3^0)$ is below the EWSB minima. Combining the results of Figs. 1 and 14 we can understand the contour in fig. 2.

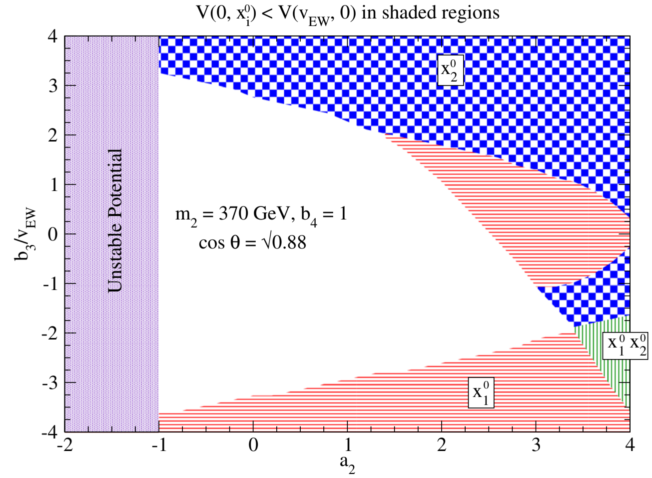

FIG. 14 (color online). Structure of the $v = 0$ vacua in the b_3 vs a_2 plane for $m_2 = 370$ GeV, $b_4 = 1$, and $\cos\theta = \sqrt{0.88}$. The different regions are where the $(v, x) = (v_{\mathrm{EW}}, 0)$ minimum lies below the $v = 0$ minima (white region), $(0, x_1^0)$ lies below $(v_{\mathrm{EW}}, 0)$ (red lined), $(0, x_2^0)$ lies below $(v_{\mathrm{EW}}, 0)$ (blue squares), and both $(0, x_2^0)$ and $(0, x_1^0)$ lie below $(v_{\mathrm{EW}}, 0)$ (green hashed).

[1] T. Plehn, M. Spira, and P. Zerwas, Nucl. Phys. **B479**, 46 (1996).
[2] U. Baur, T. Plehn, and D. L. Rainwater, Phys. Rev. D **67**, 033003 (2003).
[3] J. Baglio, A. Djouadi, R. Gröber, M.M. Mühlleitner, J. Quevillon, and M. Spira, J. High Energy Phys. 04 (2013) 151.
[4] S. Dittmaier *et al.* (LHC Higgs Cross Section Working Group), arXiv:1101.0593.
[5] R. Frederix, S. Frixione, V. Hirschi, F. Maltoni, O. Mattelaer, P. Torrielli, E. Vryonidou, and M. Zaro, Phys. Lett. B **732**, 142 (2014).
[6] M. J. Dolan, C. Englert, and M. Spannowsky, J. High Energy Phys. 10 (2012) 112.
[7] S. Dawson, S. Dittmaier, and M. Spira, Phys. Rev. D **58**, 115012 (1998).
[8] D. de Florian and J. Mazzitelli, *Proc. Sci.*, LL2014 (2014) 029 [arXiv:1405.4704].
[9] J. Grigo, K. Melnikov, and M. Steinhauser, Nucl. Phys. **B888**, 17 (2014).
[10] G. M. Pruna and T. Robens, Phys. Rev. D **88**, 115012 (2013).
[11] V. Barger, P. Langacker, M. McCaskey, M. J. Ramsey-Musolf, and G. Shaughnessy, Phys. Rev. D **77**, 035005 (2008).
[12] D. O'Connell, M. J. Ramsey-Musolf, and M. B. Wise, Phys. Rev. D **75**, 037701 (2007).
[13] S. Profumo, M. J. Ramsey-Musolf, C. L. Wainwright, and P. Winslow, arXiv:1407.5342.
[14] M. Bowen, Y. Cui, and J. D. Wells, J. High Energy Phys. 03 (2007) 036.
[15] V. Barger, L. L. Everett, C. B. Jackson, A. D. Peterson, and G. Shaughnessy, Phys. Rev. Lett. **114**, 011801 (2015).
[16] M. J. Dolan, C. Englert, and M. Spannowsky, Phys. Rev. D **87**, 055002 (2013).
[17] R. Schabinger and J. D. Wells, Phys. Rev. D **72**, 093007 (2005).
[18] C. Englert, T. Plehn, D. Zerwas, and P. M. Zerwas, Phys. Lett. B **703**, 298 (2011).
[19] C. Englert, T. Plehn, M. Rauch, D. Zerwas, and P. M. Zerwas, Phys. Lett. B **707**, 512 (2012).
[20] S. Profumo, M. J. Ramsey-Musolf, and G. Shaughnessy, J. High Energy Phys. 08 (2007) 010.
[21] J. R. Espinosa, T. Konstandin, and F. Riva, Nucl. Phys. **B854**, 592 (2012).
[22] D. Curtin, P. Meade, and C.-T. Yu, J. High Energy Phys. 11 (2014) 127.
[23] M. Gillioz, R. Grober, C. Grojean, M. Muhlleitner, and E. Salvioni, J. High Energy Phys. 10 (2012) 004.
[24] S. Dawson, E. Furlan, and I. Lewis, Phys. Rev. D **87**, 014007 (2013).

[25] C.-Y. Chen, S. Dawson, and I. Lewis, Phys. Rev. D **90**, 035016 (2014).
[26] J. Baglio, O. Eberhardt, U. Nierste, and M. Wiebusch, Phys. Rev. D **90**, 015008 (2014).
[27] B. Hespel, D. Lopez-Val, and E. Vryonidou, J. High Energy Phys. 09 (2014) 124.
[28] B. Bhattacherjee and A. Choudhury, arXiv:1407.6866.
[29] A. Arhrib, R. Benbrik, C.-H. Chen, R. Guedes, and R. Santos, J. High Energy Phys. 08 (2009) 035.
[30] N. Craig, J. Galloway, and S. Thomas, arXiv:1305.2424.
[31] J. M. No and M. Ramsey-Musolf, Phys. Rev. D **89**, 095031 (2014).
[32] J. F. Gunion, H. E. Haber, G. L. Kane, and S. Dawson, Front. Phys. **80**, 1 (2000).
[33] ATLAS Collaboration, "Constraints on New Phenomena via Higgs Boson Coupling Measurements with the ATLAS Detector.", CERN, Report No. ATLAS-CONF-2014-010, 2014.
[34] CERN Report No. ATLAS-CONF-2013-067, 2013 (unpublished).
[35] CMS Collaboration, S. Chatrchyan *et al.*, Eur. Phys. J. C **73**, 2469 (2013).
[36] S. Dawson and W. Yan, Phys. Rev. D **79**, 095002 (2009).
[37] ATLAS Collaboration, G. Aad *et al.*, arXiv:1406.5053.
[38] CMS Collaboration, CERN Report No. CMS-PAS-HIG-13-032, 2014 (unpublished).
[39] CMS Collaboration, CERN Report No. CMS-PAS-HIG-14-013, 2014 (unpublished).
[40] C. Quigg, arXiv:1101.3201.
[41] B. W. Lee, C. Quigg, and H. Thacker, Phys. Rev. D **16**, 1519 (1977).